2. Experimental

Details on the chemicals used in the experiments have been included in this chapter. The present chapter also provides an in-depth explanation of all the synthetic procedures, experimental methods and physicochemical and electrochemical characterization techniques used during the study.

2.1. Materials and Reagents

Table 2.1 provides an overview of the chemicals and reagents utilized in the experiments. All the compounds were used exactly as received without further purification. Millipore water was used to conduct the experiments.

Table 2.1: List of Chemicals

Chemicals	Purchased from
Palladium chloride ($PdCl_2$), copper(II) chloride dihydrate ($CuCl_2 \cdot 2H_2O$), cobalt(II) chloride hexahydrate ($CoCl_2 \cdot 6H_2O$), iron(II) chloride tetrahydrate ($FeCl_2 \cdot 4H_2O$ ≥99%), ethanol (C_2H_5OH, ACS, ISO, Reag., ≥99.5%), potassium hydroxide (KOH, ≥84.0%), sodium hydroxide (NaOH, 99.0%), 2-Propanol [$(CH_3)_2CHOH$, ≥99.5 %], titron X-100, hydrazine hydrate ($NH_2NH_2 \cdot H_2O$) 80%	Merck
Nafion, Graphene nanoplatelets, 20 wt% Pt/C, 20 wt% Pd/C	Alfa Aesar
Silver nitrate ($AgNO_3$ ≥99.9%)	Rankem
Titron X-100	Himedia
Vulcan XC-72R carbon (VC)	Cabot Corporation, Navi Mumbai, as gift

2.2. Synthesis of hybrid nanoparticles (NPs)

The as-synthesized NPs were mainly synthesized via solvothermal methods.

2.2.1. Synthesis of carbon-supported PdM^1M^2 NPs (PdM^1M^2/C, M^1/M^2 = Ag, Cu): The carbon-supported trimetallic PdM^1M^2 (PdM^1M^2/C; M^1/M^2 = Ag, Cu) along with their bimetallic compositions were synthesized via typical solvothermal method [1]. Each NPs system comprises of the same amount of metal atoms and the carbon support to metals is in 80:20 ratios.

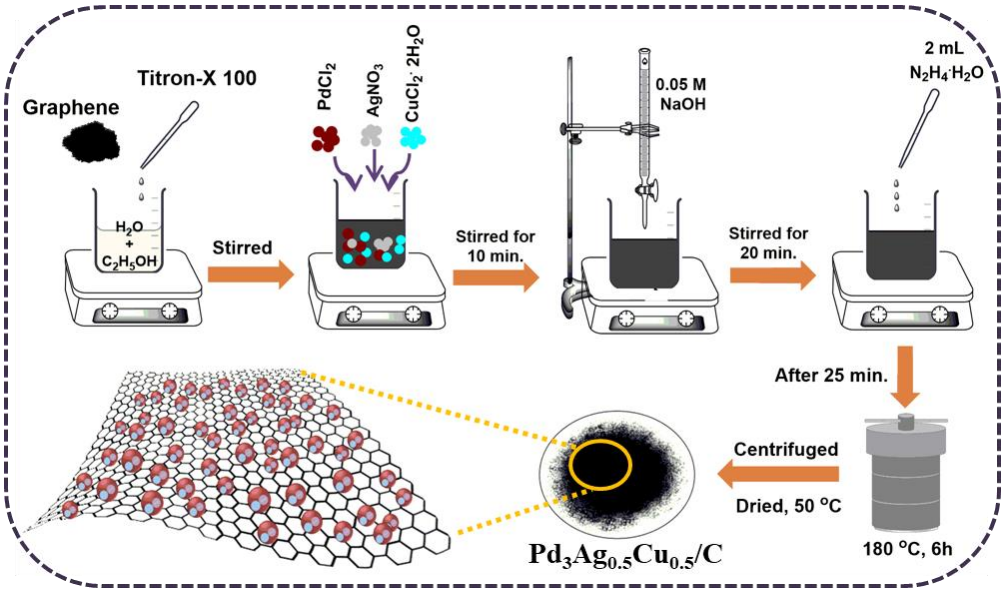

Scheme 2.1: Schematic representation of the synthesis of $Pd_3Ag_{0.5}Cu_{0.5}$/C.

2.2.1.1. Synthesis of $Pd_3Ag_{0.5}Cu_{0.5}$/C: $Pd_3Ag_{0.5}Cu_{0.5}$/C hybrid NPs were synthesized using the solvothermal method reported previously. Typically, 0.1 g of graphene NPs and 0.1 ml of Triton X-100 were added to 50 mL of the solvent system prepared by mixing distilled water and ethanol in a 1:1 ratio. The solution was stirred for 2-3 min and then 0.0328 g $PdCl_2$, 0.0052 g $AgNO_3$, and 0.0053 g $CuCl_2.2H_2O$ were added to the solution. After that, 0.05M NaOH (0.06 g in 30 mL H_2O) solution was added dropwise and stirred for 20 minutes. Subsequently, 2 mL of 85% hydrazine hydrate was added and stirred for another 25 min. The final mixture is then transferred to a 200 mL Teflon lined stainless steel autoclave and sealed it. It is then kept in an oven and maintained at a temperature of 180^{o}C for 6 h. After 6 h, it was allowed to cool to room temperature. After the required time, the product is washed and centrifuged with distilled water and ethanol to remove impurities. The final product is then collected and set to dry in a vacuum oven at 55^{o}C. The dried product is then collected and designated as $Pd_3Ag_{0.5}Cu_{0.5}$/C. The schematic illustration of the synthesis of $Pd_3Ag_{0.5}Cu_{0.5}$/C is presented in Scheme 2.1.

2.2.1.2. Synthesis of Pd_3Ag/C and $PdAg_3/C$: Pd_3Ag/C and $PdAg_3/C$ nanomaterials were synthesized via identical method as mentioned in section 2.2.1.1. All the experimental conditions were kept the same, except the molar ratio of $PdCl_2$ and $AgNO_3$ salt precursors were different. To maintain the 3:1 and 1:3 atomic ratios of Pd and Ag in Pd_3Ag/C and $PdAg_3/C$ hybrid NPs, respectively, calculated amounts of $PdCl_2$ and $AgNO_3$ were taken.

2.2.1.3. Synthesis of Pd_3Cu/C and $PdCu_3/C$: Pd_3Cu/C and $PdCu_3/C$ nanomaterials were synthesized by the identical procedure mentioned in section 2.2.1.1 by using appropriate metal precursors and maintaining the desired atomic ratios of Pd and Cu in the resultant nanomaterials. In this case, $PdCl_2$ and $CuCl_2{\cdot}2H_2O$ were calculated to maintain 3:1 and 1:3 atomic ratios of Pd and Cu in Pd_3Cu/C and $PdCu_3/C$, respectively.

2.2.1.4. Synthesis of Pd/C: The Pd/C nanomaterials were also synthesized using the similar solvothermal method as mentioned in section 2.2.1.1. In this case, an appropriate amount of $PdCl_2$ was taken as the metal precursor while maintaining the same experimental conditions.

2.2.2. Synthesis of Carbon supported Pd_2CuCo, PdCu and PdCo:

2.2.2.1. Synthesis of Pd_2CuCo/C: The 20 wt% of Cu and Co-doped Pd NPs were synthesized by the solvothermal process. In a typical synthesis, Vulcan XC-72 R (0.1 g), $PdCl_2$ (0.150 mmol, 0.0265 g), $CuCl_2{\cdot}2H_2O$ (0.075 mmol, 0.0127 g), and $CoCl_2{\cdot}6H_2O$ (0.075 mmol, 0.01781 g) were dispersed in a 50 mL of an ethanol+water (1:1 ratio) solution. A black-colored mixture was obtained, stirred on a magnetic stirring plate for 15 min and then ultrasonicated for another 5 min. To the solution, 30 mL of NaOH solution (0.05 M) was added dropwise under constant stirring and stirred vigorously for another 20 min. After that, 2 mL of 80% $NH_2NH_2{\cdot}6H_2O$ was added drop by drop with continuous stirring for up to 25 min. The mixture was poured into a 150 mL Teflon vessel, transferred to a stainless steel autoclave, and then treated at 180 °C for 6 h in a hot-air oven. After the required time, the autoclave was cooled at room temperature. The final product was centrifuged and rinsed multiple times with Millipore water and C_2H_5OH to wash out the unreacted NaOH and Cl^- and then dried in a vacuum oven at 55°C. The pH

of the solution is close to 7. The resultant material is denoted as Pd_2CuCo/C. The overall synthesis procedure of the Pd_2CuCo/C is illustrated in Scheme 2.2.

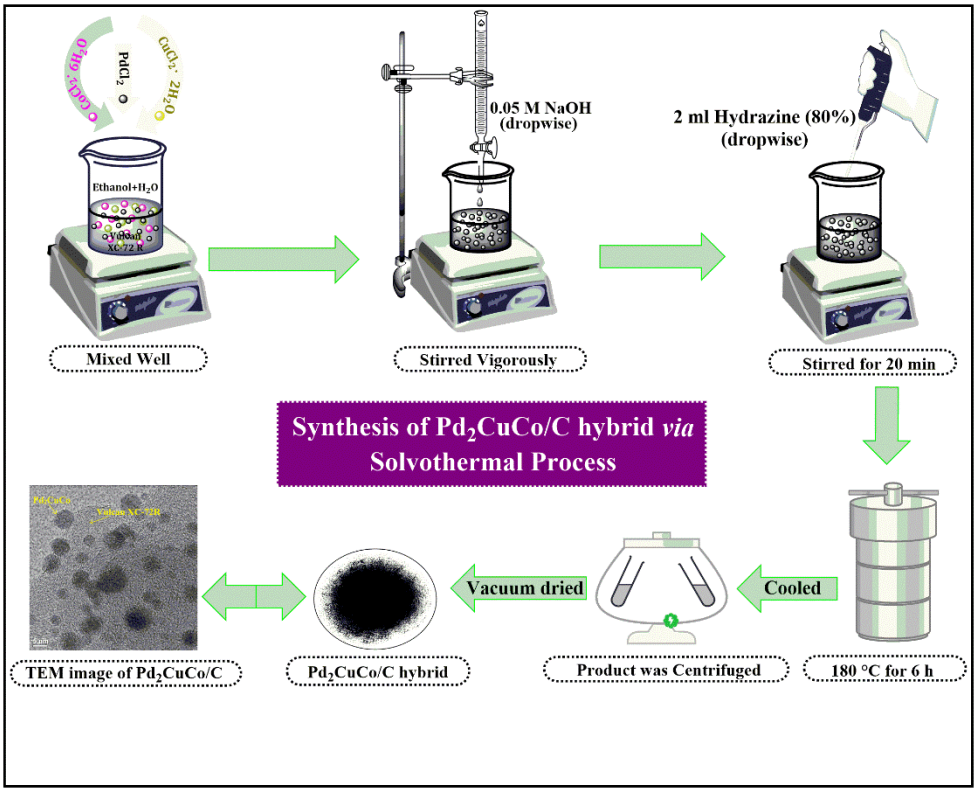

Scheme 2.2: Schematic representation of the synthesis of Pd_2CuCo/C.

2.2.2.2. Synthesis of PdCu/C: PdCu/C hybrid NPs were synthesized by a similar solvothermal method. For Cu doped Pd/C, Vulcan XC-72 R (0.1 g), $PdCl_2$ (0.150 mmol, 0.0265 g), and $CuCl_2{\cdot}2H_2O$ (0.150 mmol, 0.0254 g) were taken, and rest of the procedure is similar to the as mentioned in the section 2.2.2.1.

2.2.2.3. Synthesis of PdCo/C: In the case of Co-doped Pd/C, Vulcan XC-72R (0.1 g), $PdCl_2$ (0.150 mmol, 0.0265 g), and $CoCl_2{\cdot}2H_2O$ (0.150 mmol, 0.3562 g), were taken and the identical solvothermal procedure is followed similar to the as mentioned in the section 2.2.2.1.

2.2.3. Synthesis of Carbon supported PdFeCu, PdFe and PdCu hybrid NPs:

2.2.3.1. Synthesis of PdFeCu/C: The 20 wt% PdFeCu NPs were synthesized using the standard solvothermal procedure. To synthesize the sample, 0.110 mmol $PdCl_2$ (0.0196 g), 0.110 mmol $FeCl_2{\cdot}4H_2O$ (0.0220 g), 0.110 mmol $CuCl_2{\cdot}2H_2O$ (0.0188 g), and 0.1 g Vulcan XC-72 R were added progressively with steady stirring to a mixed solution of distilled water (25 mL) and C_2H_5OH (25 mL). Next, 30 mL of NaOH solution (0.05 M, 0.2 g) was added drop by drop at room temperature under continual stirring after the mixed solution was ultrasonicated for 10 min. After about 20 minutes, 2 mL of $NH_2NH_2{\cdot}H_2O$ was dropped into that solution and stirred continuously for another 25 min. The resulting solution was then transferred into a Teflon cup in a stainless-steel autoclave. The autoclave was then sealed and placed in a hot air oven at 125 °C for 6 h before being allowed to cool at room temperature. The final product was washed multiple times with millipore water before being washed with 50 % C_2H_5OH to eliminate unreacted NaOH and Cl^- ions and then dried in a vacuum oven at 55 °C for further studies. Scheme 2.3 illustrates the schematic synthesis procedure of PdFeCu/C.

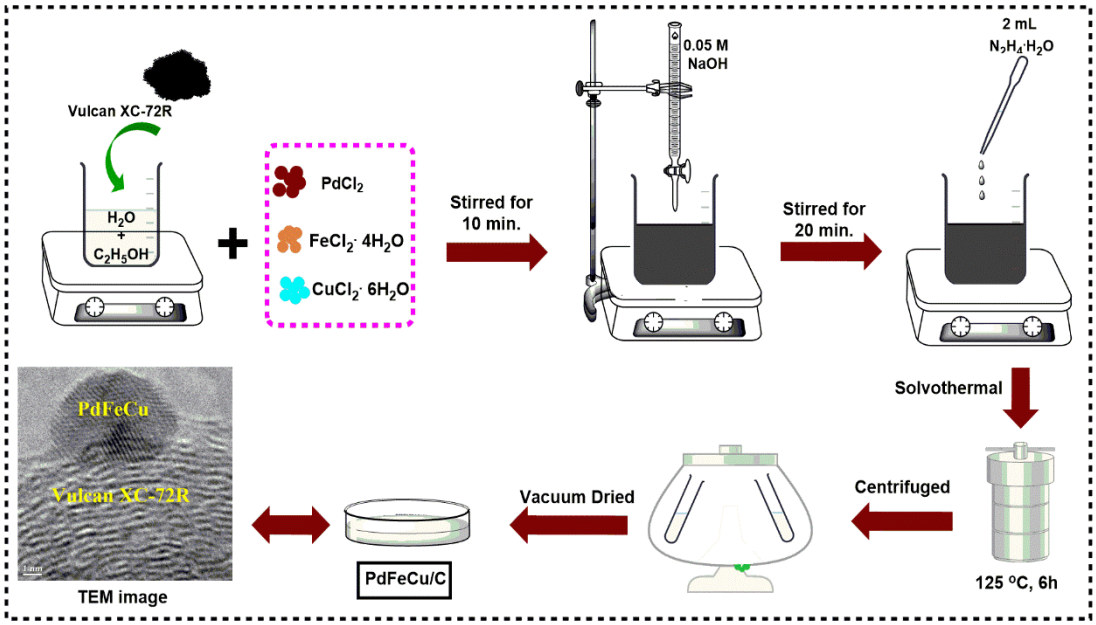

Scheme 2.3: Schematic representation of the solvothermal synthesis of PdFeCu/C.

2.2.3.2. Synthesis of PdFe/C: A similar procedure, covered in section 2.2.3.1, was also used to synthesize PdFe/C, employing $PdCl_2$ and $FeCl_2{\cdot}4H_2O$ as the precursor salt while maintaining the same experimental conditions.

2.2.3.3. Synthesis of PdCu/C: A similar procedure, covered in section 2.2.3.1, was also used to synthesize PdCu/C, employing $PdCl_2$ and $CuCl_2{\cdot}2H_2O$ as the precursor salt while maintaining the identical experimental conditions.

2.2.4. Synthesis of $PdCuO_X/C$, CuO_X/C, $PdCuO_X$ and CuO_X:

2.2.4.1. Synthesis of $PdCuO_X/C$: To synthesize, $PdCuO_X/C$ hybrid NPs 2 M (2.506g) of $CuCl_2{\cdot}2H_2O$ and 0.002 M (0.026g) of $PdCl_2$ was dispersed in 50 mL of Millipore water and EtOH (1:1 ratio) solution. Under vigorous stirring in this mixture, 30 mL of 1 M NaOH solution was added dropwise using a burette. After that, 0.025 M of ascorbic acid was added and stirred for 15 min. The resulting solution was then shifted to a Teflon-lined stainless-steel autoclave and maintained in a hot air oven at 120 °C for 6 h. After cooling to room temperature, the obtained precursors were washed with Millipore water and absolute ethanol by centrifugation and dried at 60 °C. Graphene nanoplatelets were added to the $PdCuO_X$ in a 20% weight ratio and ground for 1h in an agate mortar. After 60 minutes of grinding, the mixture was ultrasonicated with ethanol acting as a solvent, and the mixture was dried at 50 °C to obtain $PdCuO_X/C$. The schematic synthesis procedure of $PdCuO_X/C$ is illustrated in Scheme 2.4.

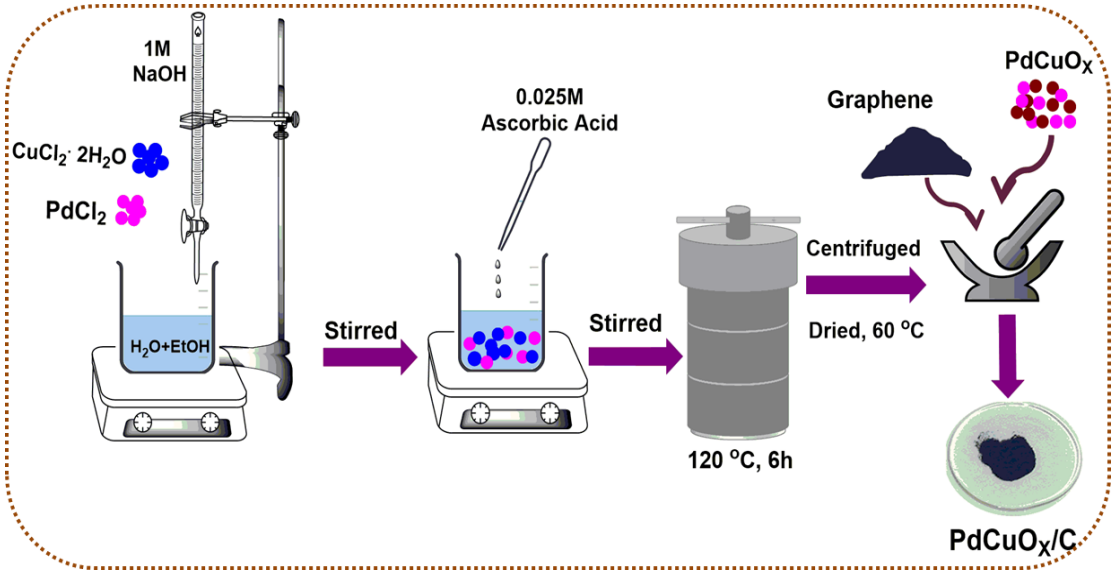

Scheme 2.4: Schematic representation of the solvothermal synthesis of $PdCuO_X/C$ hybrid NPs.

2.2.4.2. Synthesis of CuO_x/C: CuO_X/C was synthesized following the identical procedure as described in 2.2.4.1 without modifying the experimental setup and using $CuCl_2 \cdot 2H_2O$ as salt precursor.

2.2.4.3. Synthesis of $PdCuO_X$: $PdCuO_X$ NPs were synthesized following the identical method described in 2.2.4.1. $PdCl_2$ and $CuCl_2 \cdot 2H_2O$ were taken as salt precursors while maintaining all other experimental setups unaltered except avoiding the addition of graphene support.

2.2.4.4. Synthesis of CuO_X: CuO_X NPs were synthesized following the identical method as described in 2.2.4.1. $CuCl_2 \cdot 2H_2O$ was taken as a salt precursor while maintaining all other experimental setups unaltered except avoiding the addition of graphene support.

2.3. Characterization Techniques

Several analytical approaches were used to characterize the as-synthesized NPs to explore their physical and chemical properties, which are briefly discussed in the following subsections.

2.3.1. Scattering-Based Techniques for Material Characterization

2.3.1.1. Powder X-Ray Diffraction (p-XRD)

X-ray diffraction (XRD) is a highly sophisticated, non-destructive technique that gives valuable information on the amorphous and crystalline phase of the unit cell as well as provides structural details such as cell parameters, crystallite size, etc. [1, 2] The material that will be analysed must be finely ground and homogenous. Furthermore, this technique sheds light on the interplanar distance, determined by applying Bragg's equation,

$$n\lambda = 2d\sin\theta \qquad (1)$$

where, λ= wavelength of incident radiation, θ = the angle of incidence of the X-ray, d= the interplanar distance between atomic layers and n = an integer indicates that indicates the order of reflection.

The XRD working principle relies on constructive interference formed during the interaction of the incident rays with the materials and complies with Bragg's law. The

diffracted X-rays have been processed and counted after they were detected at various angles. The intensity, position and width of the peak give essential information about the materials [2, 4]. The position and intensity of the peaks are compared for confirmation using the reference diffraction patterns available from the International Centre for Diffraction Data (ICDD, earlier recognized by the Joint Committee on Powder Diffraction Standards (JCPDS) [2,4]. The average crystallite size (D) of the materials can be determined using the following Scherrer equation:

$$D = K\lambda/\beta_{2\theta}\cos\theta \qquad (2)$$

where, λ is the wavelength of the X-ray source, θ is the angle of diffraction, $\beta_{2\theta}$ is the integral breadth of the most intense peak, also known as FWHM, and K is the function of the shape of crystallite.

The p-XRD patterns of all the synthesized materials in the current investigation were recorded on a Bruker AXS Model D8 focus instrument using a nickel-filtered CuK_α radiation source with λ = 0.15418 nm within the 2θ range of 20° to 80°. The corresponding scan rate was 0.05° s^{-1}.

2.3.1.2. Raman Scattering

Raman spectroscopy is a widely used nondestructive technique to determine the functional groups, phase transitions and defects present in the materials [5-7]. The Raman effect is generated by incoming photons exchanging energy with the molecule's vibrational energy levels [5-7]. When laser light is focused onto a sample, it scatters in an inelastic manner known as Raman scattering. This occurs when energy is transferred from the excitation light to the material. Raman scattering happens when a molecule's polarizability changes due to its molecular motion. One of Raman spectroscopy's most significant benefits is the ability to deliver important information rapidly and easily with the least amount of sample handling problems. This analytical technique can also distinguish ordered and disordered carbon in carbon-supported nanoparticles. Typically, two peaks, the D- and G-bands, are observed in all carbon-containing materials at roughly 1350 and 1580 cm^{-1}, respectively. The disordered sp^3-hybridized graphitic carbon (denoted by D band) and the vibration indexed to sp^2-hybridized graphitic carbon (denoted by G band), respectively [8, 9]. A characteristic strong peak around 2700 cm^{-1} is observed in the second order D (G*)-band, the signature nature of graphitic sp^2 materials, produced by a second order resonance process [8, 9]. In this investigation, a 514 nm laser

(Ar^+ ion) with 5 mW laser intensity was used as the excitation source to record the Raman spectra of the materials.

2.3.2. Electron Microscopy Based Techniques for Material Characterization

The primary technique of electron microscopy that will be discussed is Transmission Electron Microscopy (TEM). These methods use an accelerated beam of high energy electrons to generate a high-resolution image (HRTEM).

2.3.2.1. Transmission Electron Microscopy (TEM) and High-resolution TEM (HRTEM)

TEM is the most widely used characterization technique to determine the morphology, size, structure, uniformity and distribution of NPs. TEM operates on the same fundamental principles as a light microscope, except it uses electrons rather than light. In TEM, an electron beam with a high energy of 60–120 keV passes through a thin layer of the sample on a copper grid, interacting with the sample's atoms. In contrast to TEM, HR-TEM employs a distinct methodology that produces a higher resolution and can structurally characterize materials at the atomic level [10, 11]. Typically, structures of this size are quite challenging to describe and visualize. The SAED pattern from the TEM image helps to acquire information on crystallinity as well as the presence of defects and interfaces of the materials. TEM (HRTEM) images were acquired on a JEM-2100 and JEM-100 CX II instrument with an accelerating voltage of 200 kV in 50 kV steps and 100 KV in 20 KV steps, respectively. Before imaging, the specimens were ultrasonicated in ethanol and the resulting suspension was dropcasted onto the carbon coated Cu grid and dried at room temperature [12].

2.3.3. X-Ray Based Techniques for Material Characterization

The X-ray based techniques that will be covered are X-Ray Photoelectron Spectroscopy (XPS) and Energy Dispersive X-Ray Spectroscopy (EDS or EDX).

2.3.3.1. X-Ray Photoelectron Spectroscopy (XPS)

XPS is a widely used technology that provides information on the elements and the composition and chemical oxidation state of materials within the 10 nm range. It also has a detection sensitivity that ranges from 0.1-1 atomic percentage for all the elements

excluding He and H. It operates in extremely high vacuum and is based on the photoelectric effect. Additionally, the depth sensitivity through XPS can be achieved by angle-resolved photoemission or by adjusting the photon energy with synchrotron radiation. The chemical and valence states of the core-ionized atoms are reflected in the binding energies (BEs) of XPS and XPS satellite peaks. When properly evaluated, BE shifts deliver insights about a material, which is needed to comprehend the catalytic properties of materials [13-15]. In this study, a Shimadzu ESCA-3400 system equipped with an Mg-anode X-ray cannon (10 kV, 20 mA) and Thermo Scientific ESCALAB Xi^+ spectrometer (UK) equipped with a monochromator Al Kα X-ray source (1486.6 eV) at a pressure $<10^{-7}$ Torr and an electron take-off angle of 90° was used to conduct XPS. All the samples were Ar-etched for 60 seconds prior to the measurements. All samples' BEs were calibrated against the adventitious carbon peak at 284.6 eV throughout the data processing. After baseline correction, all of the high resolution spectra were fitted into its components using Gaussian peaks. During baseline correction, a Shirley−type background was subtracted from the signals. The Savitzky−Golay method was used to smooth the XP spectra by employing a window of 10 points. A survey scan was carried out using pass energy of 200 eV to identify possible impurities and 50 eV for high resolution XPS spectrum of each element.

2.3.3.2. Energy Dispersive X-Ray Spectroscopy (EDS or EDX)

Energy-dispersive X-ray spectroscopy (EDS) is widely used to investigate the composition of elements and distribution (mapping) in nanomaterials. Measurements are performed at high energy and the EDS detector is integrated into TEM and SEM systems. High-energy electron beams are bombarded toward the surface of the material, where one electron is ejected out of the inner shell, leaving a hole in its place. An X-ray photon is emitted when the energy from a higher state is shifted to the lower state, and the EDS detector detects it. The emitted X-rays can be identified by each component found in the material and shown as spectra or mapping [16, 17]. In this study, the EDX pattern and the elemental mapping were acquired using the "JEOL, JSM Model 6390 LV," an instrument attached to the scanning electron microscope.

2.3.4. Other Techniques

2.3.4.1. Thermogravimetric Analysis (TGA)

Thermogravimetry is the area of thermal analysis that studies how the weight of material varies at a given temperature or time. The fundamental idea behind thermogravimetric analysis (TGA) is the ability to examine the weight of a sample change under controlled conditions. As a result, TGA is primarily used to understand specific thermal phenomena, including sublimation, reduction, oxidation, vaporization, adsorption, and desorption [18]. The weight change pattern is recorded when the specimen is carefully exposed to a heating or cooling atmosphere. The phrase isothermal mode and scanning mode refers to a weight change of a sample that is obtained with respect to time and temperature, respectively [18]. The Shimadzu Model TGA-50 Thermal Analyser was used to collect the TGA data for this experiment. Carbon supported Pd-based NPs were heated to 600 or 700^{o}C in air atmosphere and the heating rate was maintained at 10 ^{o}C min^{-1} for all the samples.

2.3.4.2. Fourier Transform Infrared (FTIR) Spectroscopy

FTIR analysis was done to investigate the functional groups and metal-oxygen bonds present in the NPs. It involves determining how infrared radiation interacts with a sample, whether solid, liquid, or gas. Both the frequencies and the intensities of the sample's absorptions are determined. Since chemical functional groups absorb different radiation frequencies, the frequencies can be used to determine the chemical composition [19, 20]. The absorption intensity can be used to assess the component's concentration. The present study obtained IR spectra of the NPs using a Nicolet Impact I-410 FTIR spectrophotometer by forming the sample's pellets using potassium bromide (KBr).

2.4. Electrochemical Characterization

In this thesis, a three-electrode system was used to perform the electrochemical experiments at room temperature with an Autolab potentiostat (PGSTAT204 workstation) to investigate the electrocatalytic activities of the synthesized NPs. The electrochemical measurement of the synthesized NPs were obtained via cyclic voltammetry (CV), linear sweep voltammetry (LSV) and chronoamperometry (CA), using a rotating disk electrode (RDE). The electrochemical tests were conducted at room temperature (25°C) in a three-electrode cell where Ag/AgCl (3 M KCl) was the reference electrode and Pt wire was a

counter electrode. To fabricate the working electrode, the catalyst ink was prepared with an ultrasonic mixture of catalyst, water, 2-propanol, and Nafion solutions for 30 min. The geometrical surface area of GCE is 0.0705 cm^2.

2.4.1. Cyclic Voltammetry (CV)

CV is a widely employed electroanalytical technique that helps to investigate the quantitative and qualitative information of redox reactions of molecular species, including reaction mechanisms, electrochemical kinetics, electrocatalytic processes and reversibility of the reaction. The potential of a stationary WE could be applied linearly at a steady rate of potential scanning throughout the CV measurement. A CV also known as the current-potential graph is produced by measuring the current that results from the transfer of electrons at an active reaction site with an applied voltage. An electrochemical cell that contains three electrodes and a reference electrolyte is used to perform CV. A standard three electrode system is presented in Figure 2.1 and the role of each electrode is described briefly as follows [21-24]:

Reference Electrode (RE):

The most important component of a three-electrode system is RE. The voltage window of the electrode and the pH of the electrolyte determine which REs are best for an electrochemical experiment. It is used to determine the potential of the working electrode. An ideal RE should have a steady potential, obey the Nernst equation, be reversible after electrochemical measurement (back to its standard potential), be non-polarizable and have the inner solid electrode component sparingly dissolve in the solution of electrolytes. Some typically used REs for electrochemical measurement are silver-silver chloride electrode (Ag/AgCl), mercury-mercury oxide electrode (Hg/HgO, MMO), and saturated calomel electrode (SCE).

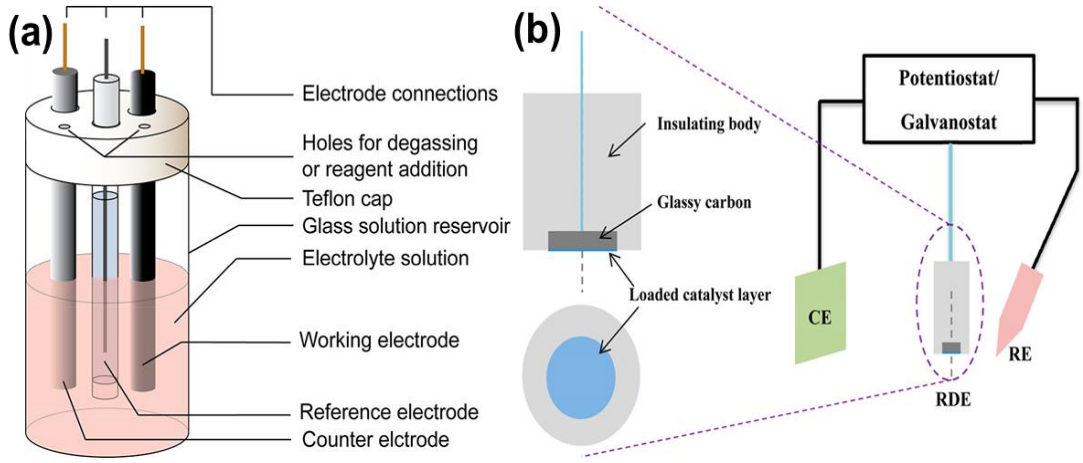

Figure 2.1: (a) Schematic representation of an electrochemical cell for CV experiments (Reproduced from Reference [21]), (b) schematic diagram of typical rotating-disk electrode (RDE) testing setup in three-electrode configuration. Catalysts are loaded on an embedded glassy carbon disc of RDE. CE and RE are acronyms of counter electrode and reference electrode, respectively (Reproduced from Reference [22]).

Working Electrode (WE):

It provides a surface at which an electrochemical reaction occurs. In a Working Electrode, the potential is controlled, and the current is recorded in response. The RDE, which serves as the WE primarily, is composed of particularly conducting carbon materials, for instance, glassy carbon (GC), pyrolytic carbon, and graphite) and noble metals (gold, platinum, etc.). In this study, we used GC electrode as the WE.

Counter electrode (CE):

The vital component of completing a three-electrode electrochemical system is counter electrodes (CE) or auxiliary electrodes (AE). The primary function of the CE is to determine the amounts of current generated when the analyte is being reduced or oxidized when the potential is being applied to WE. The geometrical surface area of the CE needs to be greater than the surface area of the WE to verify that the kinetics of the reaction occurring at the CE do not hinder those occurring at the WE. Pt wire or Pt mesh is commonly used as the CE. Carbon-based CEs such as graphite CEs are also widely employed these days.

2.4.2. Rotating Disk Electrode (RDE)

In a three-electrode system, an RDE is a hydrodynamic working electrode and that rotates to induce an analyte flow towards the electrode while doing analysis. Analyte flow can be varied by varying the electrode's rotation rate. It is the conventional hydrodynamic electroanalytical method for limiting the thickness of the diffusion layer and is applied to most electrochemical analyses to investigate the kinetics of the reactions as well as the mass transfer effects [23]. In ORR measurement, the rate at which O_2 and electrolyte diffuse towards the electrode surface is determined by RDE. In contrast to the CV, the LSV plots are recorded at a fixed sweep rate in a single potential sweep direction, either forward or backward using RDE [23, 25-27].

2.4.3. Chronoamperometry (CA)

Chronoamperometry is an electrochemical technique in which current is recorded as a function of time by constantly applying wave potential on the working electrode. The measured current fluctuates as the diffusion layers of the analyte change from the bulk solution to the electrode surface [28, 29]. Herein, a CA test was performed to check the electrostability of the catalysts towards the ORR in the identical electrochemical workstation as the CV and LSV analyses were performed. The CA analysis was carried out in 0.1 M KOH solution for 6 h at a constant potential of 0.53 V or 0.66V *vs.* RHE.

2.4.4. Supporting Electrolyte

The electrochemical measurement can be conducted in a solution phase during the electrochemical investigations and this solution is known as a supporting electrolyte. The acidic aqueous or alkaline aqueous electrolytes are used as supportive electrolytes under the N_2 or O_2-atmosphere and provide mobile ionic species that enable electrical interaction. The electrochemical reactions' kinetics were estimated by considering the supporting electrolyte's pH value, kinematic viscosity and diffusion coefficient [23]. Herein, we used 0.1 M KOH as the supporting electrolyte for electrochemical reactions.

2.4.5. Electrode Fabrication and Electrochemical Activity towards ORR

To fabricate the working electrode, the catalyst ink was prepared with an ultrasonic mixture of 5 mg catalyst, 0.2 mL Millipore water, 0.3 mL propanol, and 10 µL 5wt% of Nafion solutions for 30 min. Before each dropcasting, the GCE was polished

with 0.3-μm Al_2O_3 powder many times to get a shiny and smooth surface. In total, 3.0 μL homogeneous "ink" was slowly dropped on the GCE surface uniformly and then allowed to dry at a temperature 35 ^oC for 6 h in a vacuum oven (Figure 2.2). All electrochemical measurements were conducted in an N_2 and O_2-saturated atmosphere, to obtain an inert and oxygen-rich environment, respectively.

CV analyses were performed in N_2- and O_2-saturated environments with a scan rate of 50 mVs^{-1} in the potential range of 0.2–(–0.8) (*vs.* Ag/AgCl) in 0.1 M KOH solution. Before each electrochemical analysis, the WE was cycled several times till a reproducible CV was achieved to remove unwanted surface contamination. After that surface, the final CV curves were obtained in the respective atmosphere.

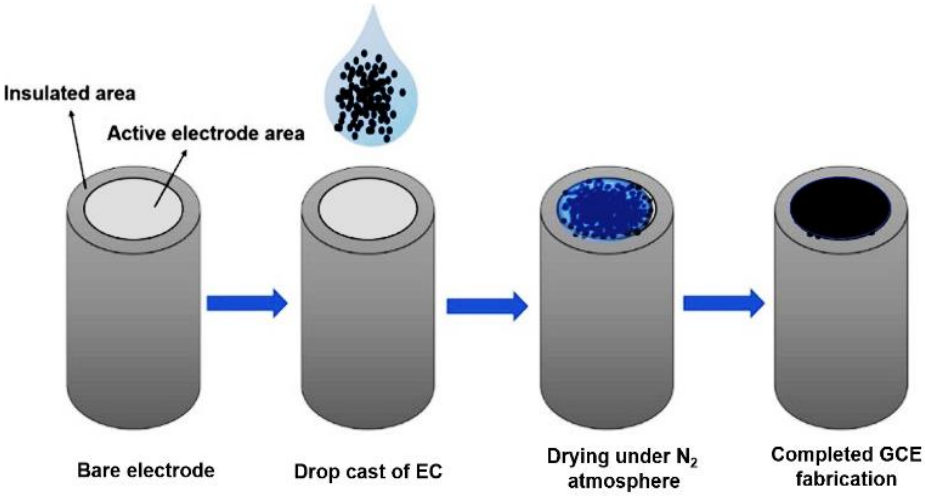

Figure 2.2: Diagrammatic representation of the fabrication of electrocatalyst over GCE (Reproduced from Reference [30]).

The same dropcasted WEs were then employed for the LSV measurement attached to the identical electrochemical system. LSV curves were achieved in the same potential window of CV. These measurements were made at different rotating rates ranging from 400-3600 rpm in an O_2-saturated 0.1 M KOH solution at a sweep rate of 10 mVs^{-1}. Prior to LSV measurement, oxygen was purged through the electrolyte for roughly 30 minutes, and the electrolyte was continually bubbled with oxygen during the experiment to keep the O_2 saturation constant. The resulting currents were normalized for each sample to the GCE's geometric surface area. To check the changes in ORR performance due to the use of Pt as CE which is believed to do electrodissolution of Pt in solution and the potential shift due to the use of Ag/AgCl, we repeated the analysis using Hg/HgO (filled with 0.1M KOH) and graphite electrode as the RE and CE, respectively.

No change in current density and potential were observed for all the electrocatalysts. All the potentials were converted with respect to a reversible hydrogen electrode (RHE) using the Nernst equation: $E_{RHE} = E_{Ag/AgCl} + E^{o}_{Ag/AgCl} + 0.059$ pH and $E_{RHE} = E_{Hg/HgO} + E^{o}_{Hg/HgO} + 0.059$ pH [1, 31] where, $E_{Ag/AgCl}$ is Ag/AgCl electrode potential and $E^{o}_{Ag/AgCl}$ is standard Ag/AgCl electrode potential at 25 °C and its value is 0.1976 V while $E_{Hg/HgO}$ is calomel electrode potential and $E^{o}_{Hg/HgO}$ is standard mercury electrode potential at 25 °C and its value is 0.163 V at a pH of 13 (0.1 M KOH) [32].

These LSV curves at various rotation rates are used to calculate the Koutecky-Levich (K-L) plot using the following equation and equation 3 is used to determine the overall electron transfer number during the ORR process [1, 31, 33, 34].

$$1/j = 1/j_L + 1/j_K = 1/B\omega^{1/2} + 1/j_k \quad (3)$$

$$\text{where, } B = 0.629nFC_o(D_o)^{2/3}\nu^{-1/6}$$

$$j_K = nFkC_o$$

where, j = current density, j_k= kinetic current density, j_l= diffusion limited current density, B = slope of the K–L plot, ω = rotating rate of the RDE (rad/s), n = number of e^- transfer per O_2 molecule, F = Faraday constant (96485 C mol^{-1}), D_{O2} = diffusion coefficient of O_2 (1.9×10^{-5} cm^{-2} s^{-1}), v = kinematic viscosity (0.01 cm^{-2} s^{-1}) and C_{O2} = bulk concentration of O_2 (1.1×10^{-6} mol cm^3) in 0.1M KOH and k = electron transfer rate constant.

The long-term stability of materials was estimated through CA measurement. CA analyses were carried out in O_2-saturated KOH solution (0.1 M) at a rotation rate of 1600 rpm for 6 h at -0.40 V *vs.* Ag/AgCl. The accelerated durability test (ADT) was conducted by cycling the potential between −0.15-(−0.45 V) *vs.* Ag/AgCl at a scan rate of 500 mVs^{-1} for 10000 cycles in an O_2-saturated 0.1M KOH solution. The LSV was measured at 1600 rpm both before and after 10,000 redox CV cycles in this experiment. The methanol tolerance was evaluated by adding methanol to the electrolyte during CA measurement for 3600s.

The ECSA reflects the surface area associated with the electronic interaction between the catalyst's and the electrolyte's surfaces during the non-faradaic reaction. The ECSA for Pd-based catalysts was calculated using the area of the PdO reduction peak on the CV curve in the N_2 atmosphere. The CVs were measured in the potential range of 0.2-

(–0.8) (*vs.* Ag/AgCl) sweep rate of 50 mVs^{-1}. The following equation (3) is used to calculate ECSA [1, 35, 36]:

$$ECSA\ (m^2\ g^{-1}) = Q/SL \quad (3)$$

where, L is the loading of Pd, Q is the charge estimated from PdO stripping, and S is a constant equal to 424μCcm^{-2} considering the surface is covered with a PdO monolayer.

The ECSAs of the metal oxide based catalysts were calculated using the double-layer capacitance (C_{DL}). To obtain C_{DL}, the CV curve in an N_2-saturated atmosphere must be used to identify a non-Faradaic range where redox reactions don't occur. The value of C_{DL} is obtained by plotting half of the anodic current−cathodic current (ja−jc/2) against the scan rate [37, 38]. The double-layer charging current is the current obtained in this non-Faradaic range. Then CV in the non-faradaic region was acquired at different scan rates of 10, 20, 30, 40, 50 and 60 mV/s. The following formula (equation 4) is used to determine ECSA [31, 37, 38]:

$$ECSA = \frac{C_{DL}}{C_S} \quad (4)$$

where, C_S is specific capacitance and its value is 40 μFcm^{-2} for a flat surface.

References

[1] Chetry, R., Chutia, B., Patowary, S., Borah, B.J., Sudarsanam, P. and Bharali, P. Electronic modulation of Pd/C by simultaneous doping of Cu and Co tendering a highly durable and methanol-tolerant oxygen reduction electrocatalyst. *Energy & Fuels*, 37(13):9557-9567, 2023.

[2] Epp, J., X-ray diffraction (XRD) techniques for materials characterization. In Altpeter I. Tschuncky R. Herrmann H. G. Hubschen G. *Materials characterization using nondestructive evaluation (NDE) methods*, Chap 4, pages 81-124, ISBN:978-0-08-100040-3. Woodhead Publishing. 2016.

[3] Fatimah, S., Ragadhita, R., Al Husaeni, D.F. and Nandiyanto, A.B.D. How to calculate crystallite size from x-ray diffraction (XRD) using Scherrer method. *ASEAN Journal of Science and Engineering*, 2(1): 65-76, 2022.

[4] Basak, M., Rahman, M.L., Ahmed, M.F., Biswas, B. and Sharmin, N. The use of X-ray diffraction peak profile analysis to determine the structural parameters of cobalt ferrite nanoparticles using Debye-Scherrer, Williamson-Hall, Halder-

Wagner and Size-strain plot: Different precipitating agent approach. *Journal of Alloys and Compounds*, 895:162694, 2022.

[5] Moon, J., Li, M., Ramirez-Cuesta, A.J. and Wu, Z., Raman spectroscopy In Wachs, I.E., Bañares, M.A., editors, *Springer Handbook of Advanced Catalyst Characterization*, pages 75-110, ISBN:978-3-031-07124-9. Springer Handbooks. Springer, Cham, 2023.

[6] Dresselhaus, M.S., Jorio, A., Souza Filho, A.G. and Saito, R. Defect characterization in graphene and carbon nanotubes using Raman spectroscopy. *Philosophical Transactions of the Royal Society A: Mathematical, Physical and Engineering Sciences*, 368(1932):5355-5377, 2010.

[7] Mulvaney, S.P. and Keating, C.D. Raman spectroscopy. *Analytical Chemistry*, 72(12):145-158, 2000.

[8] Ma, B., Rodriguez, R.D., Ruban, A., Pavlov, S. and Sheremet, E. The correlation between electrical conductivity and second-order Raman modes of laser-reduced graphene oxide. *Physical Chemistry Chemical Physics*, 21(19):10125-10134, 2019.

[9] Akhavan, O., Ghaderi, E., Hashemi, E. and Rahighi, R. Ultra-sensitive detection of leukemia by graphene. *Nanoscale*, 6(24):14810-14819, 2014.

[10] Mondal, A., Debnath, P. and Mondal, N.K., Nanoparticles: A new tool for control of mosquito larvae. In Bhattacharyya S., Platos J., Kromer P., editors, *Intelligent Environmental Data Monitoring for Pollution Management*, Chap 3, pages 49-70, ISBN:978-0-12-819671-7. Academic Press, 2021.

[11] Andreazza, P., Pierron-Bohnes, V., Tournus, F., Andreazza-Vignolle, C. and Dupuis, V. Structure and order in cobalt/platinum-type nanoalloys: from thin films to supported clusters. *Surface Science Reports*, 70(2):188-258, 2015.

[12] Baidya, T., Mazumder, T., Koltunov, K. Y., Likhar, P. R., Clark, A. H., Tiwari, K., Sobolev, V. I., Payra, S., Murayama, T., Lin, M., Bera, P., Roy, S., Biswas, K., Safonova, O., Rao, B. S., and Haruta, M. Low-temperature propylene epoxidation activity of CuO-CeO_2 catalyst with CO + O_2: Role of metal-support interaction on the reducibility and catalytic property of CuO_x species. *The Journal of Physical Chemistry C*, 124(26):14131–14146, 2020.

[13] Mourdikoudis, S., Pallares, R. M., and Thanh, N. T. Characterization techniques for nanoparticles: Comparison and complementarity upon studying nanoparticle properties. *Nanoscale*, 10(27):12871–12934, 2018.

[14] Corcoran, C.J., Tavassol, H., Rigsby, M.A., Bagus, P.S. and Wieckowski, A. Application of XPS to study electrocatalysts for fuel cells. *Journal of Power Sources*, 195(24):7856-7879, 2010.

[15] Krishna, D.N.G. and Philip, J. Review on surface-characterization applications of X-ray photoelectron spectroscopy (XPS): Recent developments and challenges. *Applied Surface Science Advances*, 12:100332, 2022.

[16] Boddolla, S., and Thodeti, S. A review on characterization techniques of nanomaterials. *International Journal of Engineering, Science and Mathematics*, 7(1):169–175, 2018.

[17] Abd Mutalib, M., Rahman, M.A., Othman, M.H.D., Ismail, A.F. and Jaafar, J. Scanning electron microscopy (SEM) and energy-dispersive X-ray (EDX) spectroscopy. In Hilal N., Fauzi Ismail A., Matsuura T. and Oatley Radcliffe D., editors, *Membrane characterization*, Chap 9, pages 161-179, ISBN:978-0-444-63776-5. Elsevier, 2017.

[18] Loganathan, S., Valapa, R. B., Mishra, R. K., Pugazhenthi, G., and Thomas, S. Thermogravimetric analysis for characterization of nanomaterials. In Thomas, S., Thomas, R., Zachariah, A. K., and Mishra, R. K., editors, *Thermal and Rheological Measurement Techniques for Nanomaterials Characterization*, volume 3 of *Micro and Nano Technologies*, pages 67–108, ISBN:978-0-323-46139-9. Elsevier, 2017.

[19] Baudot, C., Tan, C.M. and Kong, J.C. FTIR spectroscopy as a tool for nano-material characterization. *Infrared Physics & Technology*, 53(6):434-438, 2010.

[20] Bacsik, Z., Mink, J. and Keresztury, G. FTIR spectroscopy of the atmosphere. I. Principles and methods. *Applied spectroscopy reviews*, 39(3):295-363, 2004.

[21] Rountree, K. J., Mccarthy, B. D., Rountree, E. S., Eisenhart, T. T., and Dempsey, J. L. A practical beginner's guide to cyclic voltammetry. *Journal of Chemical Education*, 95:197−206, 2018.

[22] Ge, X., Sumboja, A., Wuu, D., An, T., Li, B., Goh, F.T., Hor, T.A., Zong, Y. and Liu, Z. Oxygen reduction in alkaline media: From mechanisms to recent advances of catalysts. *ACS Catalysis*, 5(8):4643-4667, 2015.

[23] Bhuvanendran, N., Ravichandran, S., Xu, Q., Maiyalagan, T. and Su, H. A quick guide to the assessment of key electrochemical performance indicators for the oxygen reduction reaction: A comprehensive review. *International Journal of Hydrogen Energy*, 47(11):7113-7138, 2022.

[24] Joshi, P. S. and Sutrave, D. S. A brief study of cyclic voltammetry and electrochemical analysis. *International Journal of ChemTech Research*, 11(9):77−88, 2019.

[25] Masa, J., Batchelor-McAuley, C., Schuhmann, W., and Compton, R. G. Koutecky–Levich analysis applied to nanoparticle modified rotating disk electrodes: Electrocatalysis or misinterpretation, *Nano Research*, 7(1):71−78, 2014.

[26] Sandford, C., Edwards, M. A., Klunder, K. J., Hickey, D. P., Li, M., Barman, K., Sigman, M. S., White, H. S., and Minteer, S. D. A synthetic chemist's guide to electroanalytical tools for studying reaction mechanisms. *Chemical Science*, 10(26):6404−6422, 2019.

[27] Evans, D. H. Review of voltammetric methods for the study of electrode reactions. In Montenegro, M. I., Queirós M. A., and Daschbach J. L., editors, Microelectrodes: Theory and applications, volume 197 of NATO ASI Series (Series E: Applied Sciences), pages 17−32, ISBN:978-94-011-3210-7. Springer-Dordrecht, 1991.

[28] Rezaei, B., and Irannejad, N. Electrochemical detection techniques in biosensor applications. In Ensafi, A. A., editor, Electrochemical biosensors, pages 11–43, ISBN:978-0-12-816491-4. Elsevier, 2019.

[29] Guy, O.J. and Walker, K.A.D. Graphene functionalization for biosensor applications. In Saddow S.E., editors, *Silicon Carbide Biotechnology*, chap 4, pages 85-141, ISBN:978-0-12-802993-0. Elsevier, 2016.

[30] Kumar, A.K.S., Zhang, Y., Li, D. and Compton, R.G. A mini-review: How reliable is the drop casting technique?. *Electrochemistry Communications*, 121:106867, 2020.

[31] Goswami, C., Yamada, Y., Matus, E.V., Ismagilov, I.Z., Kerzhentsev, M. and Bharali, P. Elucidating the role of oxide–oxide/carbon interfaces of CuOx–CeO_2/C in boosting electrocatalytic performance. *Langmuir*, 36(49):15141-15152, 2020.

[32] Kawashima, K., Márquez, R.A., Son, Y.J., Guo, C., Vaidyula, R.R., Smith, L.A., Chukwuneke, C.E. and Mullins, C.B. Accurate potentials of Hg/HgO electrodes: practical parameters for reporting alkaline water electrolysis overpotentials. *ACS Catalysis*, 13(3):1893-1898, 2023.

[33] Zhou, R., Zheng, Y., Jaroniec, M. and Qiao, S.Z. Determination of the electron transfer number for the oxygen reduction reaction: From theory to experiment. *ACS*

Catalysis, 6(7):4720-4728, 2016.

[34] Xu, S., Kim, Y., Higgins, D., Yusuf, M., Jaramillo, T.F. and Prinz, F.B. Building upon the koutecky-levich equation for evaluation of next-generation oxygen reduction reaction catalysts. *Electrochimica Acta*, 255:99-108, 2017.

[35] Sahoo, L., Garg, R., Kaur, K., Vinod, C.P. and Gautam, U.K. Ultrathin twisty PdNi alloy nanowires as highly active ORR electrocatalysts exhibiting morphology-induced durability over 200 K cycles. *Nano Letters*, 22(1):246-254, 2022.

[36] Sanij, F.D. and Gharibi, H. Preparation of bimetallic alloyed palladium-nickel electro-catalysts supported on carbon with superior catalytic performance towards oxygen reduction reaction. *Colloids and Surfaces A: Physicochemical and Engineering Aspects*, 538:429-442, 2018.

[37] Kumar, L., Chauhan, M., Boruah, P.K., Das, M.R., Hashmi, S.A. and Deka, S. Coral-shaped bifunctional $NiCo_2O_4$ nanostructure: a material for highly efficient electrochemical charge storage and electrocatalytic oxygen evolution reaction. *ACS Applied Energy Materials*, 3(7):6793-6804, 2020.

[38] Kibsgaard, J., Tsai, C., Chan, K., Benck, J.D., Nørskov, J.K., Abild-Pedersen, F. and Jaramillo, T.F. Designing an improved transition metal phosphide catalyst for hydrogen evolution using experimental and theoretical trends. *Energy & Environmental Science*, 8(10):3022-3029, 2015.